G. Di Martino, A. Iodice, D. Riccio and G. Ruello, “Filtering of Azimuth Ambiguity in Stripmap Synthetic Aperture Radar Images”, *IEEE J. Sel. Topics Appl. Earth Observ.*, vol. 7, no. 9, pp. 3967-3978, Sep. 2014. DOI: 10.1109/JSTARS.2014.2320155.

Filtering of Azimuth Ambiguity in Stripmap Synthetic Aperture Radar Images

Gerardo Di Martino, *Member, IEEE,* Antonio Iodice, *Senior Member, IEEE,*
Daniele Riccio, *Fellow, IEEE,* Giuseppe Ruello, *Member, IEEE*

Abstract — **Due to the specific characteristics of the SAR system, peculiar artifacts can appear on SAR images. In particular, finite pulse repetition frequency (PRF) and non-ideal antenna pattern give rise to azimuth ambiguity, with the possible presence of "ghosts" on the image. They are due to the replica of strong targets located outside of the antenna main beam, superposed onto low intensity areas of the imaged scene.**

In this paper we propose a method for the filtering of azimuth ambiguities on stripmap SAR images, that we name "asymmetric mapping and selective filtering" (AM&SF) method. Our framework is based on the theory of selective filtering and on a two-step procedure. In the first step, two asymmetric filters are used to suppress ambiguities due to each sidelobe of the antenna pattern, and the ratios between the original and filtered images are used to produce two maps of the ambiguity-affected areas (one for each sidelobe). In the second step, these maps are used to produce a final image in which only the areas affected by the ambiguities are replaced by their filtered (via the proper of the two filters) versions. The proposed method can be employed in situations in which similar approaches fail, and it has a smaller computational burden. The framework is positively tested on TerraSAR-X and COSMO/SkyMed SAR images of different marine scenes.

***Index Terms*— Synthetic Aperture Radar (SAR), azimuth ambiguities, radar signal processing.**

I. Introduction

SYNTHETIC Aperture Radar (SAR) images are fruitfully employed in a wide variety of applications, such as monitoring of natural disasters and maritime surveillance. However, they suffer from the well-known SAR azimuth ambiguity problem. This phenomenon is caused by the use of a finite pulse repetition frequency (PRF), combined with the fact that the azimuth antenna pattern, in practice, cannot be abruptly limited to the specified azimuth illumination beamwidth. By using the language of signal sampling theory, the azimuth antenna pattern acts as a non-ideal anti-aliasing filter, and the azimuth ambiguity can be seen as an

This work was supported by the EU-FP7 project "Development of Pre-Operational Services for Highly Innovative Maritime Surveillance Capabilities" (DOLPHIN).

The authors are with the Dipartimento di Ingegneria Elettrica e delle Tecnologie dell'Informazione, Università di Napoli Federico II, 80125, Napoli, Italy (e-mail: gerardo.dimartino@unina.it; iodice@unina.it; daniele.riccio@unina.it; ruello@unina.it).

aliasing effect. Alternatively, by using the language of antenna array design, the azimuth antenna pattern acts as the individual radiating element pattern, which should ideally suppress “grating lobes” of the (synthetic) array pattern. Azimuth ambiguity can be then seen as the effect of non-ideal suppression of grating lobes. In any case, due to this effect, on SAR images replicas (or "ghosts") of brilliant points or areas appear, that are shifted both in azimuth and (although in a smaller extent) in range. These replicas are strongly attenuated, due to the azimuth antenna beam pattern and because they are not well focused. However, if these "ghosts" are placed in a low-scattering area, such as the sea surface, they emerge with respect to the background and can be erroneously interpreted as actual targets. As a typical example, these ghosts are one of the main reasons of false alarm in ship detection applications [1]. Moreover, azimuth ambiguities can also negatively impact on the performances of interferometric applications, where they are responsible both for a coherence loss and a phase bias [2].

In the literature, two different ways are known for the suppression of azimuth ambiguities due to point targets. The first approach is based on in-phase cancellation, and it requires the estimation (using deconvolving filters) of ambiguity sources from the data, which can be hardly obtained for distributed scatterers [3]. The second approach exploits the fact that the shifts in position of the ghosts with respect to the original targets can be evaluated as a function of the radar system parameters: hence, the image can be recursively searched for ambiguities [1], [4], [5]. These methods are good candidates whenever only the ghosts due to point targets are of interest (unless further post-processing is applied [5]), as in the case of ocean scenes in low resolution images, where the typical sources of ambiguities are isolated ships, whose size is comparable with image resolution. However, in coastal zones over the sea, and also in ocean scenes in high resolution images, many ambiguities due to distributed targets are present. For these situations, methods [1], [3]-[4] are not suitable, and the use of techniques based on the concept of selective filtering has been advocated [6], [7]. These techniques use a band-pass filter to select from the whole azimuth spectrum those areas which are less affected by ambiguities, so that this approach can be applied to ghosts due to both point targets and distributed targets, although at the cost of a resolution loss. In particular, in [6] a smart method, based on adaptive Wiener filtering, has been devised to minimize the resolution loss. More recently, a method exploiting the availability of multi-polarization data has been also proposed [8]. It exploits scatterer reciprocity, which causes equality of reflectivities at HV and VH polarizations, and the fact that, due to the particular acquisition scheme of the different polarimetric channels in quad-pol SAR systems, and to corresponding further processing, in the summation of HV and VH channels the ambiguity tends to cancel out [8]. However, in the following we will focus on methods able to deal with a single polarization channel, which have a wider range of applicability.

In the present paper, similarly to what proposed in [6], a two-step procedure is presented, in which selective filtering is obtained by using Wiener filters. As in [6], the first step is aimed at identifying areas actually affected by azimuth ambiguities. However, we here show (see Section III) that the method in [6] may fail to identify ambiguities for some configurations of the

antenna pattern and PRF values actually encountered in current high resolution spaceborne SAR systems; conversely, our approach does not suffer from this problem.

Once the ambiguity map has been generated, in the second step the adaptive procedure of [6] can be employed, based on the evaluation of local signal-to-ambiguity ratios, which can also be estimated using the spectral-based method proposed in [9]. However, we here show (see Section III.B) that a much simpler (and faster) procedure is sufficient in most cases to obtain very good ambiguity filtering results. This procedure has also the advantage that it can be employed even when sources of ambiguities are outside the considered scene, at variance with the approach of [6]. For a reason that will be clear in the subsequent sections, we call our procedure "asymmetric mapping and selective filtering" (AM&SF) method.

The paper is organized as follows. In Section II the basic theory on azimuth ambiguities in SAR images is briefly recalled. In Section III.A the rationale of the proposed ambiguity filtering procedure is described, while in Section III.B the generation of the "ghost map" and of the final filtered image is detailed. Relevant experimental results are presented in Section IV, with reference to both TerraSAR-X and Cosmo/SkyMed stripmap images. Finally, conclusions are reported in Section V.

II. Azimuth Ambiguities in SAR Images

We assume that the SAR image is obtained from the raw signal through standard processing, i.e. through a matched-filter approach, and we neglect SAR system space-variance. These assumptions are inessential for the development of our method, and are here made just to simplify the introduction of the main concepts on SAR azimuth ambiguity. Let $I(\xi,\eta)$ and $H_s(\xi,\eta)$ be the Fourier transforms of the image, $i(x,r)$, and of the raw signal, $h_s(x,r)$, azimuth-sampled at rate PRF$/v$, with ξ and η being the Fourier mates of azimuth x and slant range r, respectively, v the uniform sensor velocity, and PRF the Pulse Repetition Frequency. In this case, the SAR image can be described in the Fourier domain as follows [10], [11]

$$I(\xi,\eta) = H_s(\xi,\eta)\mathrm{rect}\left[\frac{\xi-\xi_{DC}}{2a_0X}\right]\mathrm{rect}\left[\frac{\eta}{bc\tau}\right]\exp\left(j\frac{\xi^2}{4a}\right)\exp\left(j\frac{\eta^2}{4b}\right) =$$

$$\Gamma(\xi,\eta)W\left[\frac{\xi-\xi_{DC}}{2a_0r_0}\right]\mathrm{rect}\left[\frac{\xi-\xi_{DC}}{2a_0X}\right]\mathrm{rect}\left[\frac{\eta}{bc\tau}\right] + \sum_{i\neq 0}\Gamma(\xi_i,\eta)\exp\left(\frac{\xi_i^2-\xi^2}{4a}\right)W\left[\frac{\xi_i-\xi_{DC}}{2a_0r_0}\right]\mathrm{rect}\left[\frac{\xi-\xi_{DC}}{2a_0X}\right]\mathrm{rect}\left[\frac{\eta}{bc\tau}\right], \quad (1)$$

where

- $X=\lambda r_0/L$ is the effective azimuth footprint, r_0 being the closest range between the platform and the center of the footprint, λ the electromagnetic wavelength and L the azimuth antenna length;
- $a = a_0\left(1+\frac{\eta\lambda}{4\pi}\right)$, with $a_0 = \frac{2\pi}{\lambda r_0}$;

- $b = \frac{2\alpha}{c^2}$, where α is the chirp rate and *c* the speed of light;
- τ is the transmitted pulse duration;
- $\xi_i = \xi - \frac{2\pi i \mathrm{PRF}}{v}$, with *i* an integer number;
- $\xi_{DC} = \frac{2\pi}{v} f_{DC}$, f_{DC} being the Doppler centroid frequency;
- $W[\psi]$ is the two-way azimuth antenna pattern (AAP), whose effective beamwidth is $\Delta\psi = \frac{\lambda}{L} = \frac{X}{r_0}$;
- $\Gamma(\cdot)$ is the Fourier transform of the scene reflectivity, whose bandwidth is much larger than that of the SAR system.

Note that according to (1) a linear relation exists between the azimuth wavenumber and the AAP angle ψ:

$$\xi - \xi_{DC} \simeq -\frac{4\pi}{\lambda}\psi = -2a_0 r_0 \psi \,, \tag{2}$$

allowing to express $W[\psi]$ as a function of ξ and the effective azimuth bandwidth as $\Delta\xi \simeq \frac{4\pi}{\lambda}\Delta\psi = 2a_0 X = \frac{4\pi}{L}$.

Accordingly, SAR systems are designed to satisfy the condition $\frac{2\pi \mathrm{PRF}}{v} \geq 2a_0 X$, i.e. $\mathrm{PRF} \geq \frac{2v}{L}$, to avoid under-sampling of the signal effective Doppler bandwidth (indeed, $2v/L$ is the Nyquist rate of the signal).

In (1) the first term accounts for the baseband focused contribution of the target spectrum, while the second one is responsible for ambiguities, and is made up of the spectral replicas of the reflectivity folded ("aliased") into the processed bandwidth. In particular, from (1) it is evident that the AAP acts as a sort of anti-alias filter, limiting the presence of out-of-band contributions: ideally, if $W[\psi]$ were null for $|\psi| > \Delta\psi$ (i.e., no sidelobes), we would have $W\left[\frac{\xi_i - \xi_{DC}}{2a_0 r_0}\right] \mathrm{rect}\left[\frac{\xi - \xi_{DC}}{2a_0 X}\right] = 0$ for $i \neq 0$, so that the second term in (1) would be null, and no azimuth ambiguity would be present. In practice, this condition can be only approached (by using an antenna with a high peak-to-sidelobe ratio), but it can never be exactly achieved. Therefore, azimuth ambiguity is always present. However, it is negligible, except, possibly, in areas where the baseband focused contribution of the target spectrum (the "true" signal) is very low.

With regard to the phase term in the summation in (1), using the expressions of ξ_i and a_0 reported above, and assuming that $\left(1 + \frac{\eta\lambda}{4\pi}\right)^{-1} \simeq \left(1 - \frac{\eta\lambda}{4\pi}\right)$, we can write

$$\exp\left(\frac{\xi_i^2 - \xi^2}{4a}\right) = \exp\left(j\xi \frac{i\mathrm{PRF}\lambda r_0}{2v}\right) \exp\left(-j\frac{(i\mathrm{PRF})^2 \lambda r_0 2\pi}{4v^2}\right) \exp\left(-j\xi\eta \frac{i\mathrm{PRF}\lambda^2 r_0}{8\pi v}\right) \exp\left(j\eta \frac{(i\mathrm{PRF})^2 \lambda^2 r_0}{8v^2}\right). \tag{3}$$

The first phase term in (3) is responsible for the azimuth displacement of *i*-th order azimuth ambiguities, given by

$$\Delta x_i = i\frac{\mathrm{PRF}\lambda r_0}{2v}, \tag{4}$$

which, if the PRF is equal to the Nyquist rate of the azimuth signal, i.e. PRF=2v/L, reduces to $\Delta x_i = iX$, i.e. an integer multiple of the azimuth footprint. The second exponential term is an inessential constant phase term, while the last one accounts for the range displacement of the i-th order azimuth ambiguity, given by

$$\Delta r_i = \frac{\Delta x_i^2}{2r_0}, \tag{5}$$

where the expression in (4) has been used. Finally, the third phase term is responsible for a slight defocusing of replicas and a residual wavenumber-dependent migration. Note that this third phase term is proportional to the square of the wavelength, so that ghosts defocusing is more relevant at low frequency. Therefore, this is one of the reasons why azimuth ambiguity appears more easily on images obtained by high-frequency (i.e., X-band) sensors. Another reason is the fact that at high frequencies data dynamic is much higher and point and man-made targets are much brighter with respect to sea clutter.

In conclusion, in the presence of low-reflectivity areas (a typical example is the sea surface) ghosts can appear, due to the presence of high-reflectivity target replicas displaced according to (4) and (5), weighted by the sidelobes of the AAP, and slightly defocused. In (1)-(5) the spectral replicas of any order are considered. However, replicas of order higher than one are most often negligible, so that in the following we limit our attention to first-order replicas only, i.e. those due to the first folded sidelobe segments of the spectrum, obtained by setting $i = \pm 1$. Substituting (3) in (1) we get

$$I(\xi,\eta) = \Gamma_0(\xi,\eta)W_0[\xi,\eta] + \Gamma_+(\xi,\eta)W_+[\xi,\eta] + \Gamma_-(\xi,\eta)W_-[\xi,\eta]\,, \tag{6}$$

where

$$W_0[\xi,\eta] = W\left[\frac{\xi-\xi_{DC}}{2a_0r_0}\right]\mathrm{rect}\left[\frac{\eta}{bc\tau}\right]\mathrm{rect}\left[\frac{\xi-\xi_{DC}}{2a_0X}\right] \tag{7}$$

$$W_+[\xi,\eta] = W\left[\frac{\left(\xi-\frac{2\pi\mathrm{PRF}}{v}\right)-\xi_{DC}}{2a_0r_0}\right]\mathrm{rect}\left[\frac{\eta}{bc\tau}\right]\mathrm{rect}\left[\frac{\xi-\xi_{DC}}{2a_0X}\right]\exp\left(j\xi\frac{\mathrm{PRF}\lambda r_0}{2v}\right)\exp\left(-j\frac{\mathrm{PRF}^2\lambda r_0 2\pi}{4v^2}\right)\exp\left(-j\xi\eta\frac{\mathrm{PRF}\lambda^2 r_0}{8\pi v}\right)\exp\left(j\eta\frac{\mathrm{PRF}^2\lambda^2 r_0}{8v^2}\right) \tag{8}$$

$$W_-[\xi,\eta] = W\left[\frac{\left(\xi+\frac{2\pi\mathrm{PRF}}{v}\right)-\xi_{DC}}{2a_0r_0}\right]\mathrm{rect}\left[\frac{\eta}{bc\tau}\right]\mathrm{rect}\left[\frac{\xi-\xi_{DC}}{2a_0X}\right]\exp\left(-j\xi\frac{\mathrm{PRF}\lambda r_0}{2v}\right)\exp\left(-j\frac{\mathrm{PRF}^2\lambda r_0 2\pi}{4v^2}\right)\exp\left(j\xi\eta\frac{\mathrm{PRF}\lambda^2 r_0}{8\pi v}\right)\exp\left(j\eta\frac{\mathrm{PRF}^2\lambda^2 r_0}{8v^2}\right), \tag{9}$$

and Γ_0, Γ_+, and Γ_- are $\Gamma(\xi_i, \eta)$ for $i = 0, +1, -1$ respectively, i.e., the reflectivities of the unambiguous and ambiguous targets.

III. Azimuth Ambiguity Filtering

The approach used in this paper for ambiguity filtering is based on the concept of selective filtering, i.e. on frequency-domain nulling of ambiguity energy [6], [7]. Essentially, in the frequency domain we select the region of the signal spectrum less affected by aliasing, i.e., the region where the nulls of the folded AAP are located (in fact, the spectrum of the scene reflectivity is weighted by the AAP of the sensor, so that where the folded AAP presents a null, the spectrum of the ambiguity will be null, whatever the original shape of reflectivity spectrum). In a way similar to that of [6], we obtain the transfer function (TF) of the filter using the theory of Wiener filtering, as shown in the following sub-section. Once the TF of the filter is available, we propose a filtering approach based on the generation of "ghost maps", which are then used to get the final filtered image, where only the areas affected by the ambiguities are substituted with their filtered version, as detailed in Section III.B.

A. Filter synthesis

Wiener filters are particularly well-suited to deal with the problem at hand. The goal is to evaluate the TF of a filter which, through the use of *N* azimuth samples of the image, is able to filter out the ambiguities, minimizing the mean square error between the "true" unambiguous signal and the filtered one (i.e., we deal with an MMSE problem). We consider here a one-dimensional problem, treating separately each fixed-range line of the (complex) SAR image. For this reason, in the following the dependence on the η variable is omitted. Starting from the one-dimensional version of (6), we can define the unambiguous signal I_0 and the ambiguous data X, also affected by an additive white thermal noise T, as

$$I_0(\xi) = \Gamma_0(\xi) W_0[\xi] \tag{10}$$

$$X(\xi) = \Gamma_0(\xi) W_0[\xi] + \Gamma_+(\xi) W_+[\xi] + \Gamma_-(\xi) W_-[\xi] + T(\xi)\,. \tag{11}$$

Now we can evaluate the power spectral densities associated to the unambiguous and ambiguous targets as follows

$$S_0(\xi) = \mathrm{E}\left[I_0[\xi] I_0^{*}[\xi]\right] = \mathrm{E}[|\Gamma_0[\xi]|^2]|W_0[\xi]|^2 = \sigma_0 |W_0[\xi]|^2 \tag{12}$$

$$S_+(\xi) = \mathrm{E}[|\Gamma_+[\xi]|^2]|W_+[\xi]|^2 = \sigma_+ |W_+[\xi]|^2 \tag{13}$$

$$S_-(\xi) = \mathrm{E}[|\Gamma_-[\xi]|^2]|W_-[\xi]|^2 = \sigma_- |W_-[\xi]|^2, \tag{14}$$

where E[·] stands for "statistical mean" and σ_0, σ_+, and σ_- are the power spectral densities of the reflectivity relevant to the unambiguous and to the two ambiguous targets, respectively. Note that they can be considered to be independent of the azimuth wavenumber ξ in the processed bandwidth. In writing the expressions in (12)-(14), we also implicitly assume that reflectivity is statistically stationary within the filter spatial extent, *N*. In this case, the expression of the Wiener filter is [6], [12]:

$$H(\xi) = \frac{\mathrm{E}[I_0(\xi)X^*(\xi)]}{\mathrm{E}[X(\xi)X^*(\xi)]}\ , \tag{15}$$

where * stands for complex conjugate. Considering the expressions in (10)-(14) and assuming that ambiguous and unambiguous data are zero-mean and uncorrelated, from (15) we get:

$$H(\xi) = \frac{S_0(\xi)}{S_0(\xi)+S_+(\xi)+S_-(\xi)+\sigma_t} = \frac{\sigma_0|W_0(\xi)|^2}{\sigma_0|W_0(\xi)|^2+\sigma_+|W_+(\xi)|^2+\sigma_-|W_-(\xi)|^2+\sigma_t}\ , \tag{16}$$

where σ_t is the white thermal noise power density. Equation (16) can be rewritten as

$$H(\xi) = \left(1 + \frac{\sigma_+}{\sigma_0}\frac{|W_+(\xi)|^2}{|W_0(\xi)|^2} + \frac{\sigma_-}{\sigma_0}\frac{|W_-(\xi)|^2}{|W_0(\xi)|^2} + \frac{\sigma_t}{\sigma_0}\frac{1}{|W_0(\xi)|^2}\right)^{-1}. \tag{17}$$

Ratios σ_+/σ_0 and σ_-/σ_0 are not a priori known. In [6], starting from the result in (17), it is assumed as a worst case that they are both very large, i.e. $\sigma_+ = \sigma_- = \sigma \gg \sigma_0$. In this case we get[1]

$$H(\xi) = \frac{\sigma_0}{\sigma}\left(\frac{|W_+(\xi)|^2+|W_-(\xi)|^2}{|W_0(\xi)|^2} + \frac{\sigma_t}{\sigma}\frac{1}{|W_0(\xi)|^2} + \frac{\sigma_0}{\sigma}\right)^{-1}, \tag{18}$$

where the sum of the last two terms is very small (we assumed it is −60 dB), but cannot be omitted in order to avoid singularities in the filter TF, which can occur whenever the first term approaches zero. However, the assumption of equal power for both ambiguities may imply that the filter in (18) is not adequately selective in the frequency domain, thus providing poor filtering results in several practical situations. This happens when the AAP and PRF value are such that the peak of one folded AAP sidelobe locates almost exactly in correspondence of the null of the other one. We verified that this may be the case for many current high resolution spaceborne SAR sensors, e.g. TerraSAR-X and Cosmo/SkyMed. As an example, in Fig. 1 (a) the first

[1] Note that in [6] some inessential typos led to a slightly different expression for the filter in (18).

sidelobes of the AAP folded into the azimuth processed bandwidth are shown, while in Fig. 1 (b) the filter TF resulting from the definition in (18) is presented. It can be noted that the filter TF obtained through (18) is almost uniform in the processed bandwidth.

In [6] the filter in (18) is used in a preliminary step for the identification of areas affected by ambiguity and for the estimation of the local signal-to-ambiguity ratios, in particular for the estimation of σ_0. Hence, whenever a situation as the one depicted in Fig. 1 occurs, the algorithm of [6] fails to identify the ambiguity areas. Starting from this observation, we developed a different filtering approach, assuming that in each pixel only the ambiguity due to one folded sidelobe is present, and its power is much larger than the power related to the unambiguous signal. This means that we either assume that $\sigma_+ \gg \sigma_0$ and $\sigma_- = 0$, so that (17) becomes

$$H_+(\xi) = \frac{\sigma_0}{\sigma_+}\left(\frac{|W_+(\xi)|^2}{|W_0(\xi)|^2} + \frac{\sigma_t}{\sigma_+}\frac{1}{|W_0(\xi)|^2} + \frac{\sigma_0}{\sigma_+}\right)^{-1}, \tag{19}$$

or, conversely, that $\sigma_- \gg \sigma_0$ and $\sigma_+ = 0$, so that from (17) we get

$$H_-(\xi) = \frac{\sigma_0}{\sigma_-}\left(\frac{|W_-(\xi)|^2}{|W_0(\xi)|^2} + \frac{\sigma_t}{\sigma_-}\frac{1}{|W_0(\xi)|^2} + \frac{\sigma_0}{\sigma_-}\right)^{-1}. \tag{20}$$

We refer to the filters defined by these TFs as “asymmetric filters”. Note that similar filters are used in [9] for the evaluation of the local azimuth-ambiguity-to-signal-ratio (AASR). If we process the image with both the filters in (19) and (20), we obtain two filtered images, in each of which the ambiguities due to one different AAP sidelobe are filtered out. In this way, we are able to identify ambiguities due to both sidelobes, i.e., due to sources located on both sides of the considered target. In Fig. 2, where the filter TFs $H_+$and H_- obtained using the same TerraSAR-X AAP considered in Fig. 1 are shown, it is possible to appreciate the huge increase in frequency selectivity with respect to Fig. 1 (b). The filters (19) and (20) can be efficiently evaluated in the frequency domain, provided that all the required sensor parameters (AAP, PRF, f_{DC}, v, λ) are known. Note that the inessential constant factor $\sigma_0/\sigma_\pm$ in the TFs (18)-(20) can be ignored, and that in (18)-(20) only the moduli of W_0 and $W_\pm$ appear, so that the complex exponential factors in (7)-(9) play no role in the filters' TFs[2]. Once back-transformed in the spatial domain, the impulse response can be truncated to a limited number of samples ($N \simeq 30$) and convolved with each image azimuth line. The details on

[2] We note that the effectiveness of filters (19) and (20) is dependent on the PRF. In fact, the PRF dictates the position of the null of the first sidelobe folded into the processed bandwidth, which in turn determines the azimuth ambiguity attenuation. In particular, the maximum ambiguity attenuation is obtained when the null is located in correspondence of the point of maximum of the AAP, i.e. at zero frequency.

the procedure allowing to obtain the final filtered image by combining the two filtered images obtained via the filters in (19) and (20) are reported in the next sub-section.

Finally, we note that the assumptions leading to (19) and (20) are reasonable in most practical cases: in fact, the most common situations in which the problem of ambiguities arises are relevant to the sea surface, and they are usually due to only one single AAP sidelobe. The eventuality of a superposition in the same area of azimuth ambiguities due to both sidelobes represents a limiting case, which can occur, for instance, in marine gulfs, channels, and straits: in these scenarios, when for a pixel $\sigma_+ \simeq \sigma_-$, both our approach and the one presented in [6] fail to filter out the ghosts in the common situation depicted in Fig.1.

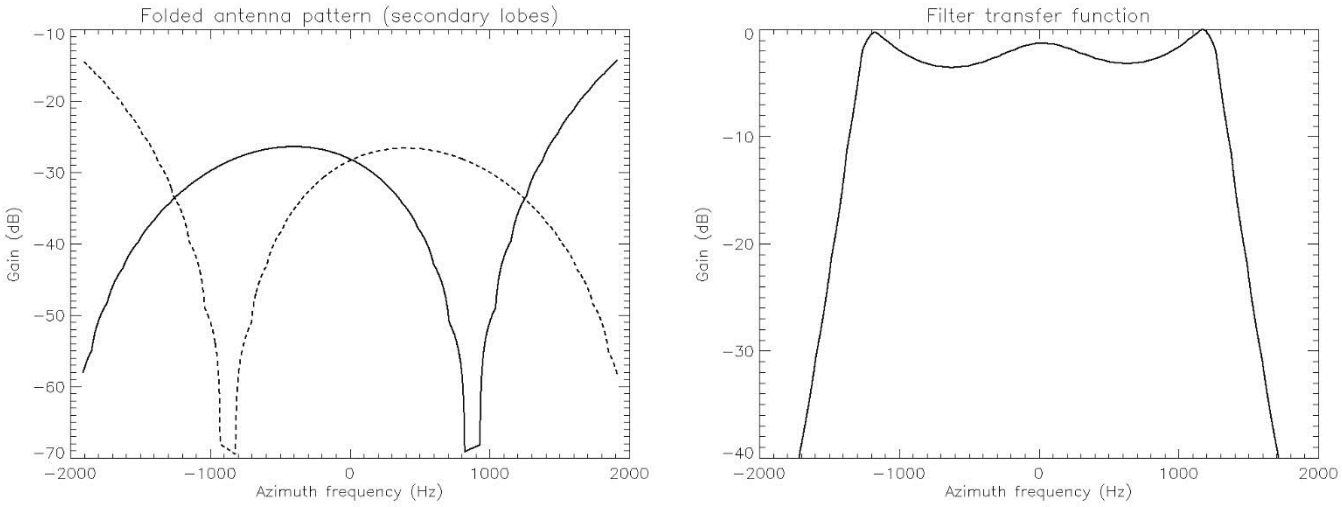

(a) (b)

Fig. 1: First sidelobes of the AAP folded into the processed azimuth bandwidth (a) and filter TF H (b), in the case of TerraSAR-X data.

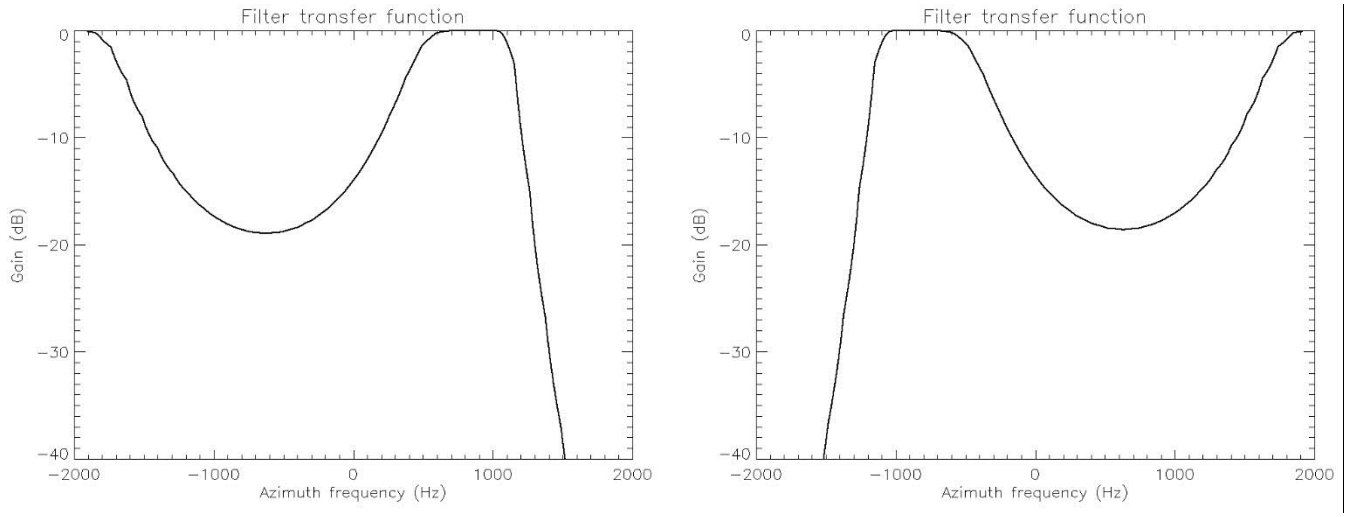

(a) (b)

Fig. 2: Filter TFs H_+ (a) and H_- (b), in the case of TerraSAR-X data.

B. Filtering rationale

In the previous sub-section the synthesis of the filters H_+ and H_- was detailed. Thanks to these filters we are able to obtain two (complex) images, $i_+(x,r)$ and $i_-(x,r)$, where "+" and "–" ambiguities are filtered out, respectively. Starting from these images, it is possible to generate two ghost maps, $b_+(x,r)$ and $b_-(x,r)$, i.e. binary maps reporting the locations of ambiguities pertaining to each sidelobe. We name $b_\pm$ "asymmetric ghost maps", since they are obtained via the "asymmetric filters". In the following we provide a description of the procedure used to obtain these ghost maps and, starting from them, the final filtered ambiguity-free image.

We start by evaluating the ratios

$$r_+(x,r) = \frac{\langle |i(x,r)|^2 \rangle}{\langle |i_+(x,r)|^2 \rangle} \frac{\mathrm{Av}\left[\langle |i_+(x,r)|^2 \rangle\right]}{\mathrm{Av}[\langle |i(x,r)|^2 \rangle]} \tag{21}$$

and

$$r_-(x,r) = \frac{\langle |i(x,r)|^2 \rangle}{\langle |i_-(x,r)|^2 \rangle} \frac{\mathrm{Av}\left[\langle |i_-(x,r)|^2 \rangle\right]}{\mathrm{Av}[\langle |i(x,r)|^2 \rangle]}, \tag{22}$$

where $\langle \cdot \rangle$ stands for spatial multilook averaging (usually, 6 to 8 samples in both azimuth and range are averaged) and $\mathrm{Av}[\cdot]$ stands for the spatial mean value computed over the entire image. Equations (21) and (22) represent the ratios between unfiltered and filtered intensity images, each normalized to its average value. Normalization is introduced to take into account the change in the mean power of the image in the areas not affected by ambiguities after filtering, so that ratios $r_\pm$ are expected to be unitary in the absence of ambiguity, and larger than 1 in areas affected by ambiguity (see the Appendix for more details). Accordingly, the ratios in (21) and (22) are thresholded in order to obtain the binary maps:

$$b_+(x,r) = \begin{cases} 1, & r_+(x,r) > r_t \\ 0, & r_+(x,r) \le r_t \end{cases} \tag{23}$$

and

$$b_-(x,r) = \begin{cases} 1, & r_-(x,r) > r_t \\ 0, & r_-(x,r) \le r_t \end{cases}, \tag{24}$$

where r_t is a real number greater than one. We verified that $r_t \simeq 2$ is a good choice in most practical situations. This is also in agreement with the theoretical considerations reported in the Appendix.

The binary maps obtained through (23) and (24), despite the multilook averaging applied in steps (21) and (22), present a residual noise component due to the presence of speckle in the SAR images: its effect mainly consists in the presence of isolated pixels wrongly detected as ghosts. This problem is tackled applying a sliding window on the binary map, setting the value of the pixels of the window to 0 if the number of non-zero pixels within the window is found to be lower than a prescribed threshold n_t, and to 1 otherwise. In the limiting case in which both b_+ and b_- are set to 1, we reasonably assume that this is caused by the speckle and we set to 0 the mask for which the corresponding value of $r_\pm$ is smaller than the other: in this way we try to identify on the masks the correct source of ambiguity. For this algorithm the parameters to be set are the sliding window size and n_t. This choice depends on a trade-off between speckle effect reduction and resolution of the ghost maps. We verified that a window size of 5x5 pixels and a threshold n_t=6 are the best values for the TerraSAR-X and Cosmo/SkyMed images used in this work.

Once the ghost maps are obtained, we can interpolate them back to full resolution and use them to obtain the final filtered image, which will be given by

$$i_{filt}(x,r) = \begin{cases} i_+(x,r)\sqrt{\frac{\mathrm{Av}[\langle|i(x,r)|^2\rangle]}{\mathrm{Av}[\langle|i_+(x,r)|^2\rangle]}}, & \text{for } (x,r) \text{ such that } b_+(x,r) = 1 \\ i_-(x,r)\sqrt{\frac{\mathrm{Av}[\langle|i(x,r)|^2\rangle]}{\mathrm{Av}[\langle|i_-(x,r)|^2\rangle]}}, & \text{for } (x,r) \text{ such that } b_-(x,r) = 1 \\ i(x,r), & \text{for } (x,r) \text{ such that } b_+(x,r) = 0 \text{ and } b_-(x,r) = 0 \end{cases}, \tag{25}$$

where the square root of the ratio between image intensity means is used to ensure mean value conservation between the original and the filtered image (see the Appendix for more details). In this way, the final filtered image will differ from the original one only in the areas affected by ambiguities. In particular, $i_{filt}(x,r)$ will keep the original resolution in all areas not affected by ambiguities, while in the rest of the image ambiguities are filtered at the expense of a slight loss in geometric resolution. The block scheme of the proposed filtering approach is shown in Fig. 3. Of course, the simple procedure described by (25) requires a much lower computational burden with respect to adaptive filtering based on the precise evaluation of the local signal-to-ambiguity ratios, but, in spite of that, obtained filtering results are very satisfactory in most cases, as shown in the next section.

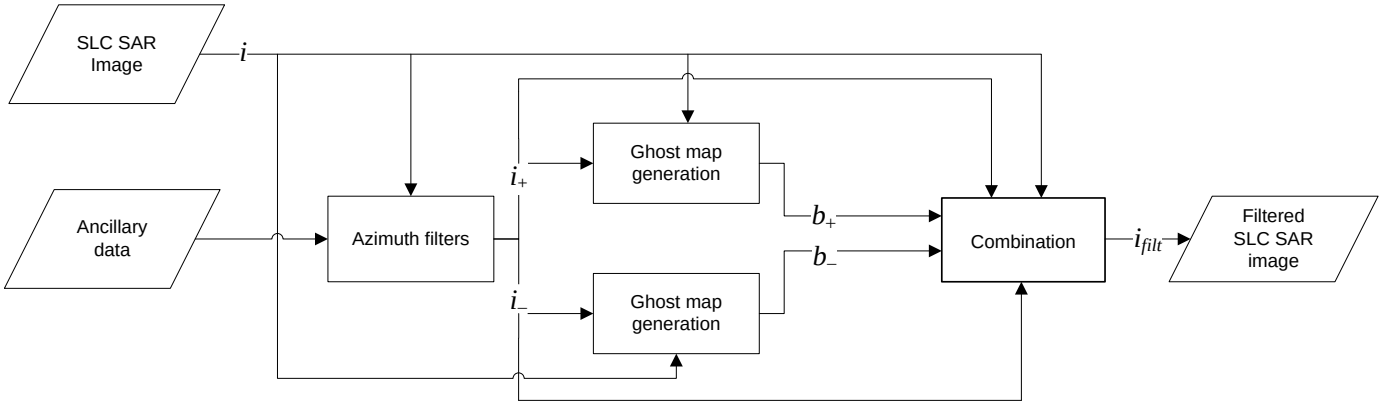

Fig. 3: Block scheme of the proposed approach.

IV. Experimental Results

The described framework has been tested on TerraSAR-X and Cosmo/SkyMed stripmap images. We selected these sensors because for them there is sometimes a combination of PRF and AAP such that the method of [6] cannot be applied, as discussed in Section III.A. In addition, as discussed in Section II, X-band sensors are more affected by ghosts due to azimuth ambiguity than lower frequency sensors.

The parameters necessary for the implementation of the filter can be retrieved from ancillary data provided together with SAR products. In the case of TerraSAR-X data the provided AAP is very detailed, including 5 sidelobes per side. Conversely, the AAP provided together with Cosmo/SkyMed data includes only part of the first sidelobes. For this reason, in this last case we had to complete the provided AAP, obtaining a worst case guess of the AAP, exploiting the knowledge of the guaranteed peak-to-sidelobe ratio. With regard to f_{DC} values, although those of TerraSAR-X are usually lower than Cosmo/SkyMed ones, they are always located in the baseband. The acquisition parameters relevant to the data-set presented in the present work are listed in Table I. In this Table CSKS1 and CSKS4 indicate sensors 1 and 4 of the Cosmo/SkyMed constellation, respectively.

In Fig. 4 (a) a stripmap TerraSAR-X image acquired close to the coast of Algeria is shown. Ambiguities (i.e., ghosts caused by azimuth ambiguity) due to the presence of the urban area in the upper part of the image are clearly visible over the sea surface and are enclosed within the red boxes. On the image in Fig. 4 (b), which is filtered according to the proposed approach, a significant reduction of the ambiguities can be noted, while no evidence of artifacts can be appreciated in the areas subject to filtering. To better illustrate the performance of our technique, in Fig. 5 a full-resolution particular of the images in Fig. 4 is presented. In the area subject to filtering only a slight decrease in resolution can be observed; conversely, in all other areas of the image no loss in resolution is experienced, as it can be noted, in particular, in the upper part of the image, where a part of the

harbor is visible. To provide a quantitative evaluation of the ambiguity reduction obtained through the proposed technique in this image, we measured the ratio between the intensity of the ghost enclosed in the yellow rectangle in Fig. 5 and the intensity of the surrounding sea area, on both original and filtered images. Results are reported in the first row of Table II, and they show an about 7 dB reduction of ghost intensity in the filtered image.

In Fig. 6 (a) a stripmap TerraSAR-X image relevant to the gulf of Naples, Italy, is shown, where an ambiguity due to a man-made structure located in the harbor is clearly visible within the red box. This kind of point-target-like ghost is particularly critical in maritime surveillance applications, because they can be easily responsible for false alarms in ship detection algorithms. In the filtered image presented in Fig. 6 (b), it can be noted that, while the ghost is filtered out, the ships present in the image are preserved, without any loss in resolution. In Fig. 7 a full-resolution particular of the ghost enclosed in the red box in Fig. 6 is shown. The ratios between the intensity of the area enclosed in the yellow rectangle in Fig. 7 and the intensity of the surrounding sea area, on both original and filtered images, are reported in the second row of Table II, and they show that also for this rather weak ghost a significant attenuation is obtained in the filtered image.

Similar results have been obtained for several Cosmo/SkyMed images of the gulf of Naples. Among these, as the most challenging case we here consider the image in Fig. 8 (a), in which many ambiguities can be observed all over the sea surface. Just in the middle of these ambiguities a ship is present (highlighted by the red box), thus providing a worst case scenario for the evaluation of the technique performances. As it can be noted from Fig. 8 (b), the proposed approach is able to filter out most of the ambiguities, while preserving the ship radar cross section. This can be better appreciated from the full-resolution particular of the image, provided in Fig. 9. In fact, Fig. 9 (b) shows that the ship signature is almost perfectly preserved, whereas surrounding ghosts are practically completely removed. For instance, for the ghost enclosed in the yellow box in Fig. 9, ratios reported in the third row of Table II show an attenuation of more than 15 dB in the filtered images, which completely cancels the ghost.

The last case is relevant to a Cosmo/SkyMed image of an area placed offshore, close to the coast of Malta. The original image is presented in Fig. 10 (a), where the presence of a ship can be appreciated at the center of the scene, along with ambiguities due to both sidelobes. On the filtered image in Fig. 10 (b) both ghosts are strongly attenuated, even if for the lower one the presence of a residual ambiguity signal can be observed. This can be better appreciated looking at Fig. 11, where full-resolution particulars of the ghosts due to both AAP sidelobes are shown. While the upper ghost is attenuated by more than 20 dB, see the fourth row of Table II, which refers to the area enclosed in the yellow rectangle in Figs. 11 (a) and 11 (b), in the lower one there is a small bright area that is not attenuated at all by filtering. However, the rest of the ghost is significantly attenuated, as shown by the fifth row of Table II, that refers to the area enclosed in the yellow rectangle in Figs. 11 (c) and 11 (d). The presence of this residual ambiguity signal can be perhaps ascribed to the non-perfect knowledge of the AAP and of the f_{DC} in case of Cosmo/SkyMed

TABLE I
SENSOR PARAMETERS FOR THE PRESENTED DATA-SET

Acquisition parameters	TerraSAR Algeria	TerraSAR Naples	Cosmo Naples CSKS4	Cosmo Malta CSKS1	TerraSAR interferometric pair master ; slave
Wavelength [m]	$3.11 \cdot 10^{-2}$	$3.11 \cdot 10^{-2}$	$3.12 \cdot 10^{-2}$	$3.12 \cdot 10^{-2}$	$3.11 \cdot 10^{-2}$
Polarization	HH	HH	HH	HH	HH
Sensor velocity [m/s]	7070	7083	6912	6956	7081
Look angle [deg]	39	29	30	36	31
PRF [Hz]	3819	3720	3333	3109	3448
f_{DC} [Hz]	–80	74	–1145	–200	–32 ; –25
Azimuth resolution [m]	3.00	3.00	2.5	3.0	3.30
Ground range resolution [m]	2.16	2.44	2.5	3.0	2.28
Acquisition date [dd/mm/yyyy]	13/12/2007	19/03/2008	01/08/2011	18/06/2013	25/04/2008 ; 17/05/2008

data. In fact, for this image, the accuracy of the Doppler Centroid provided in the ancillary data, as declared in the ancillary data themselves, is rather poor (± 115 Hz), at variance with the other images considered in this section.

Finally, in Fig. 12 we show the result obtained filtering the TerraSAR-X image in Fig. 4 (a) using the filter TF in (18), instead of our filters (19) and (20). As a matter of fact, the ambiguities present over the sea surface are still present in the filtered image. Hence, the use of this image for the generation of the ghost map, according to the procedure described in [6], will lead to miss the ghosts present on the scene.

Above examples illustrate the effect of our algorithm on amplitude images: reduction of ghosts on such images is in fact the main aim of our approach. However, of course our algorithm applies to complex images, so that it is also able to reduce the effect of azimuth ambiguity on SAR interferograms. To show this, we consider an interferometric image pair acquired by TerraSAR-X in April and May, 2008, and relative to the area of Crotone, Italy. Figure 13 (a) shows the amplitude of the master image, and Fig. 13 (b) shows the interferogram obtained from the image pair. Azimuth ambiguity manifests itself as bright ghosts on the sea area of the amplitude image, and as phase disturbances, with the appearance of spurious fringes, on the same area of the interferogram. We applied our algorithm to the two complex images of the pair: Fig. 13 (c) shows the amplitude of the filtered master image, and Fig. 13 (d) shows the interferogram obtained from the filtered images. It is evident that the effects of the ambiguity are strongly reduced on both the amplitude image and on the interferogram. In particular, the phase disturbances over the interferogram are removed, whereas the interferometric phase is not modified in the ambiguity-free areas.

To conclude this section on the experimental results, it is worth noting that the entire processing chain from the original to the final filtered image is completely unsupervised, and it is very fast: processing time is 20 seconds for an about 12000 × 9000 pixels input SLC SAR image, on a 3 GHz dual core PC, with 8 GB RAM, in normal working conditions, using non-optimized IDL™ software code. Note that processing time scales linearly with the total number of pixels.

V. CONCLUSIONS

In this paper a new effective method for the filtering of azimuth ambiguities in high resolution stripmap SAR images, the AM&SF method, has been presented. The proposed approach was developed in the framework of Wiener filtering theory. It is based on the preliminary generation of two binary ghost maps, reporting the position of ambiguities pertaining to the two first sidelobes of the AAP. Thanks to these maps we are able to restrict the filtering only to the areas actually affected by ambiguities, while keeping the original radiometric and geometric resolution in all other areas.

The proposed approach is particularly well-suited for high resolution spaceborne SAR sensors, e.g. TerraSAR-X and Cosmo/SkyMed. In fact, it overcomes the problem presented by the adaptive-filtering approach in [6], which, by preliminarily considering in each pixel the simultaneous presence of ambiguities due to both sidelobes, in some cases fails to identify correctly the areas of the image affected by ghosts.

The approach was tested on a wide data-set made up of both TerraSAR-X and Cosmo/SkyMed images, and demonstrated to provide good filtering results, both in terms of ambiguity removal and preservation of the geometric, radiometric and phase characteristics of the images. In addition, processing time is extremely low, and this is important when a huge amount of image data must be processed, as in the case of the SAR missions cited above.

It is finally appropriate to note that, as all other methods based on selective filtering, and most methods based on different concepts, our approach can be used only for the stripmap acquisition mode.

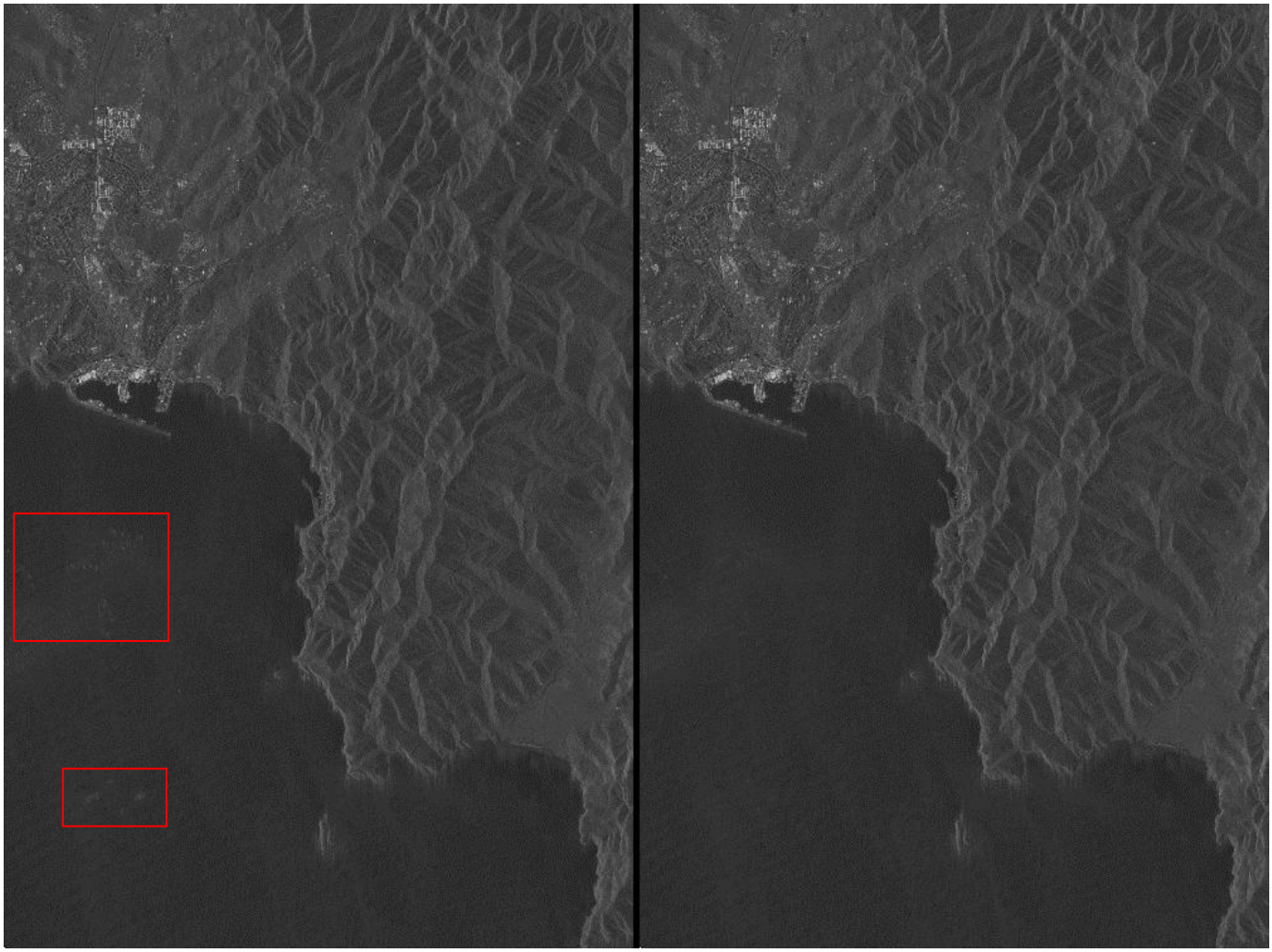

(a) (b)

Fig. 4: Original TerraSAR-X image of the coast of Algeria (a) and its filtered version (b) (a spatial multilook of 8x8 pixels is applied). Ambiguities due to buildings and man-made areas are visible over the sea surface in (a) within the red boxes, while they are strongly attenuated in (b). In this and in all subsequent figures, the same gray-level scale is used for both original and filtered images, and the near range is on the left.

APPENDIX

GHOST MAPS THRESHOLD EVALUATION

In this section we provide relevant details regarding the determination of the threshold r_t used in (23) and (24) for the generation of the two ghost masks. We start from the expression of the ratio between the power of the original image, P_X, and that of the filtered one, $P_{I_\pm}$, which can be evaluated locally on the images as:

$$\frac{P_X}{P_{I_\pm}} = \frac{\int\left(S_0(\xi)+S_\pm(\xi)\right)d\xi}{\int\left(S_0(\xi)+S_\pm(\xi)\right)\left|H_\pm(\xi)\right|^2 d\xi} = \frac{\int S_0(\xi)d\xi+\int S_\pm(\xi)d\xi}{\int S_0(\xi)\left|H_\pm(\xi)\right|^2 d\xi+\int S_\pm(\xi)\left|H_\pm(\xi)\right|^2 d\xi} \simeq \frac{\langle|i(x,r)|^2\rangle}{\langle\left|i_\pm(x,r)\right|^2\rangle}, \tag{26}$$

where the integrals are extended to the processed bandwidth. We are now interested in computing the value assumed by (26) in two particular cases, i.e. when ambiguities are not present and, vice versa, when they are present and their power is comparable to that of the unambiguous signal. In the first case, we have that $S_\pm(\xi) \simeq 0$ over the whole processed bandwidth and, hence, we get

$$\left.\frac{P_X}{P_{I_\pm}}\right|_{S_\pm(\xi)\simeq 0} \simeq \frac{\int S_0(\xi)d\xi}{\int S_0(\xi)\left|H_\pm(\xi)\right|^2 d\xi}. \tag{27}$$

In the second case, we have that $\int S_0(\xi)d\xi \simeq \int S_\pm(\xi)d\xi$, and we obtain

$$\left.\frac{P_X}{P_{I_\pm}}\right|_{\int S_0(\xi)d\xi\simeq\int S_\pm(\xi)d\xi} \simeq \frac{2\int S_0(\xi)d\xi}{\int S_0(\xi)\left|H_\pm(\xi)\right|^2 d\xi} = 2\left.\frac{P_X}{P_{I_\pm}}\right|_{S_\pm(\xi)\simeq 0}, \tag{28}$$

where the term $\int S_\pm(\xi)\left|H_\pm(\xi)\right|^2 d\xi \simeq 0$, because we assumed that $H_\pm$ ensures a strong reduction of ambiguity power. Note that, in the hypothesis that the ghosts are present only on a little portion of the image, we can obtain a good estimate of the ratio in (27) as

$$\left.\frac{P_X}{P_{I_\pm}}\right|_{S_\pm(\xi)\simeq 0} \simeq \frac{\mathrm{Av}\left[\langle|i(x,r)|^2\rangle\right]}{\mathrm{Av}\left[\langle\left|i_\pm(x,r)\right|^2\rangle\right]}, \tag{29}$$

i.e. simply evaluating the ratio between the average intensities of the original and filtered image. This is the reason why in (21) and (22) we use the reciprocal of (29) as a normalizing factor, thus obtaining

$$r_\pm\big|_{S_\pm(\xi)\simeq 0} \simeq 1, \tag{30}$$

and

$$r_\pm\big|_{\int S_0(\xi)d\xi\simeq\int S_\pm(\xi)d\xi} \simeq 2. \tag{31}$$

This implies that the choice of $r_t \simeq 2$ in (23) and (24) allows the identification of the ambiguities for which the local signal-to-ambiguity ratio is smaller than 1, which are those of most practical interest.

Finally, note that, as a consequence of the above discussion, the square root in (29) is used also to ensure mean value conservation between the original and the filtered intensity images in (25).

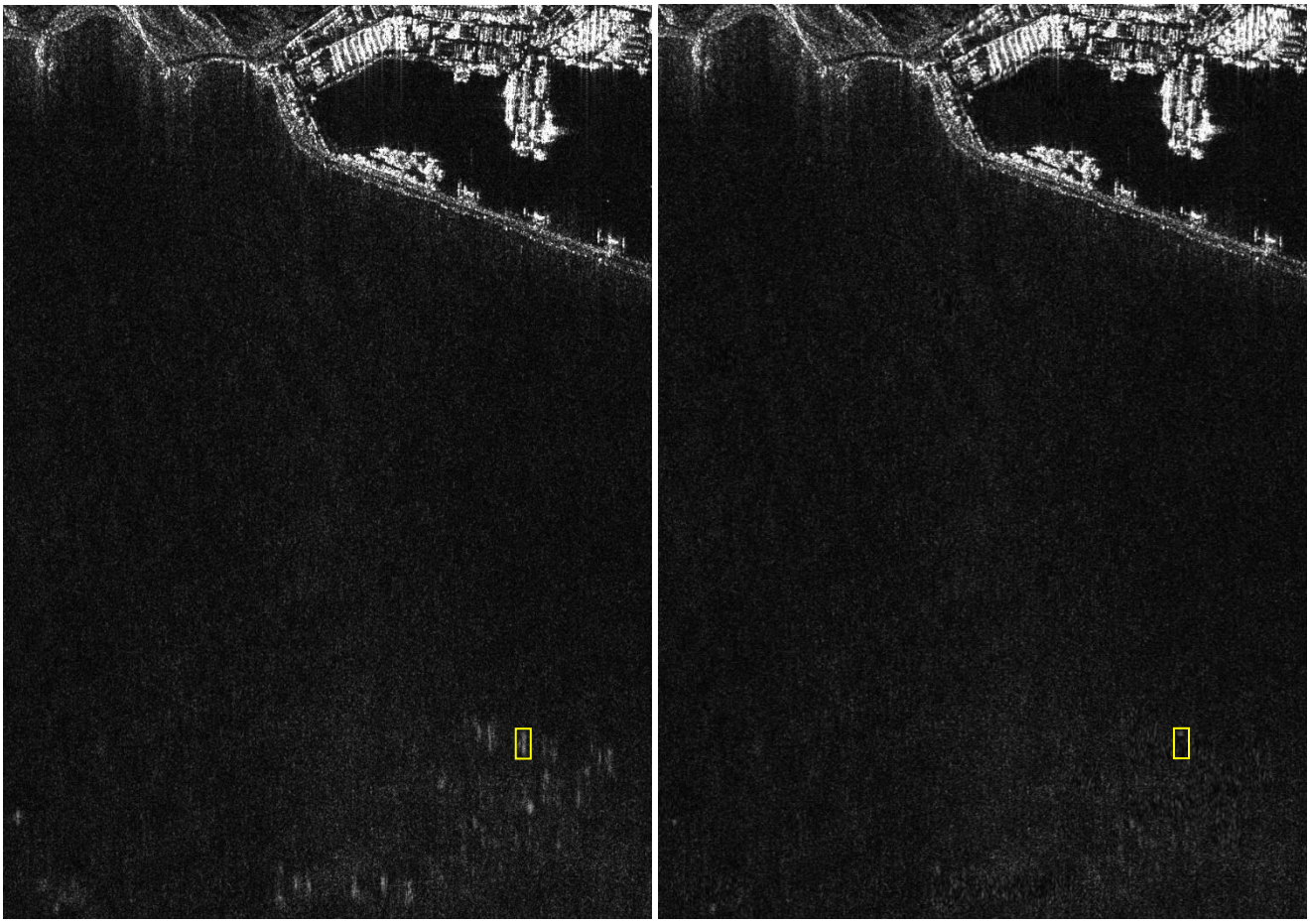

(a) (b)

Fig. 5: Full-resolution particular of the TerraSAR-X image in Fig. 4: original (a) and filtered (b) image.

REFERENCES

[1] S. Brusch, S. Lehner, T. Fritz, M. Soccorsi, A. Soloviev, and B. van Schie, "Ship Surveillance with TerraSAR-X," *IEEE Trans. Geosci. Remote Sens.*, vol. 49, no. 3, pp. 1092–1103, Mar. 2011.

[2] M. Villano and G. Krieger, "Impact of Azimuth Ambiguities on Interferometric Performance," *IEEE Geosci. Remote Sens. Lett.*, vol. 9, no. 5, pp. 896–900, Sept. 2012.

[3] A. Moreira, "Suppressing the azimuth ambiguities in synthetic aperture radar images," *IEEE Trans. Geosci. Remote Sens.*, vol. 31, no. 4, pp. 885–895, July 1993.

[4] R. K. Raney and G. J. Princz, “Reconsideration of Azimuth Ambiguities in SAR,” *IEEE Trans. Geosci. Remote Sens.*, vol. 25, no. 6, pp. 783–787, Nov. 1987.

[5] J. Chen, M. Iqbal, W. Yang, P. Wang, and B. Sun, “Mitigation of Azimuth Ambiguities in Spaceborne Stripmap SAR Images Using Selective Restoration,” *IEEE Trans. Geosci. Remote Sens.*, vol. 52, no. 7, pp. 4038–4045, July 2014.

[6] A. Monti Guarnieri, “Adaptive Removal of Azimuth Ambiguities in SAR Images,” *IEEE Trans. Geosci. Remote Sens.*, vol. 43, no. 3, pp. 625–633, Mar. 2005.

[7] F. K. Li and W. T. K. Johnson, “Ambiguities in Spaceborne Synthetic Aperture Radar Systems,” *IEEE Trans. Aerosp. Electron. Syst.*, vol. 19, no. 3, pp. 389–397, May 1983.

[8] D. Velotto, M. Soccorsi, and S. Lehner, “Azimuth Ambiguities Removal for Ship Detection Using Full Polarimetric X-Band SAR Data,” *IEEE Trans. Geosci. Remote Sens.*, vol. 52, no. 1, pp. 76–88, Jan. 2014.

[9] M. Villano and G. Krieger, “Spectral-Based Estimation of the Local Azimuth Ambiguity-to-Signal Ratio in SAR Images,” *IEEE Trans. Geosci. Remote Sens.*, vol. 52, no. 5, pp. 2304–2313, May 2014.

[10] G. Franceschetti and R. Lanari, *Synthetic Aperture Radar Processing*. New York: CRC Press, 1999.

[11] G. Franceschetti, R. Guida, A. Iodice, D. Riccio, and G. Ruello, “Efficient Simulation of Hybrid Stripmap/Spotlight SAR Raw Signal from Extended Scenes”, *IEEE Trans. Geosci. Remote Sens.*, vol. 42, no. 11, pp. 2385–2396, Nov. 2004.

[12] A. Papoulis, *Probability, Random Variables, and Stochastic Processes*. Singapore: McGraw-Hill, 1984.

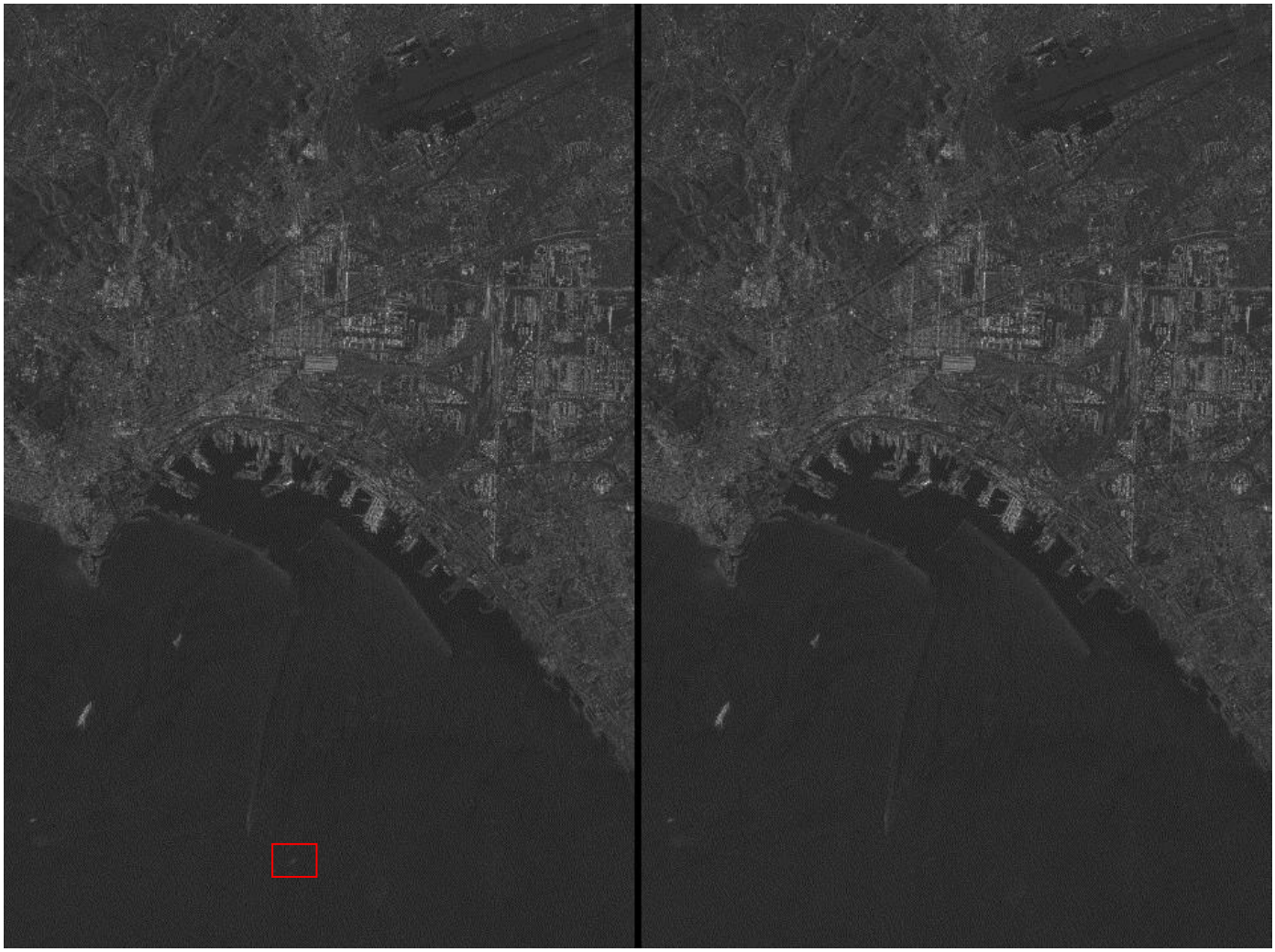

(a) (b)

Fig. 6: Original TerraSAR-X image of the gulf of Naples (a) and its filtered version (b) (a spatial multilook of 8x8 pixels is applied). An ambiguity due to an area pertaining to the harbor is visible over the sea surface in (a) within the red box, while it is strongly attenuated in (b).

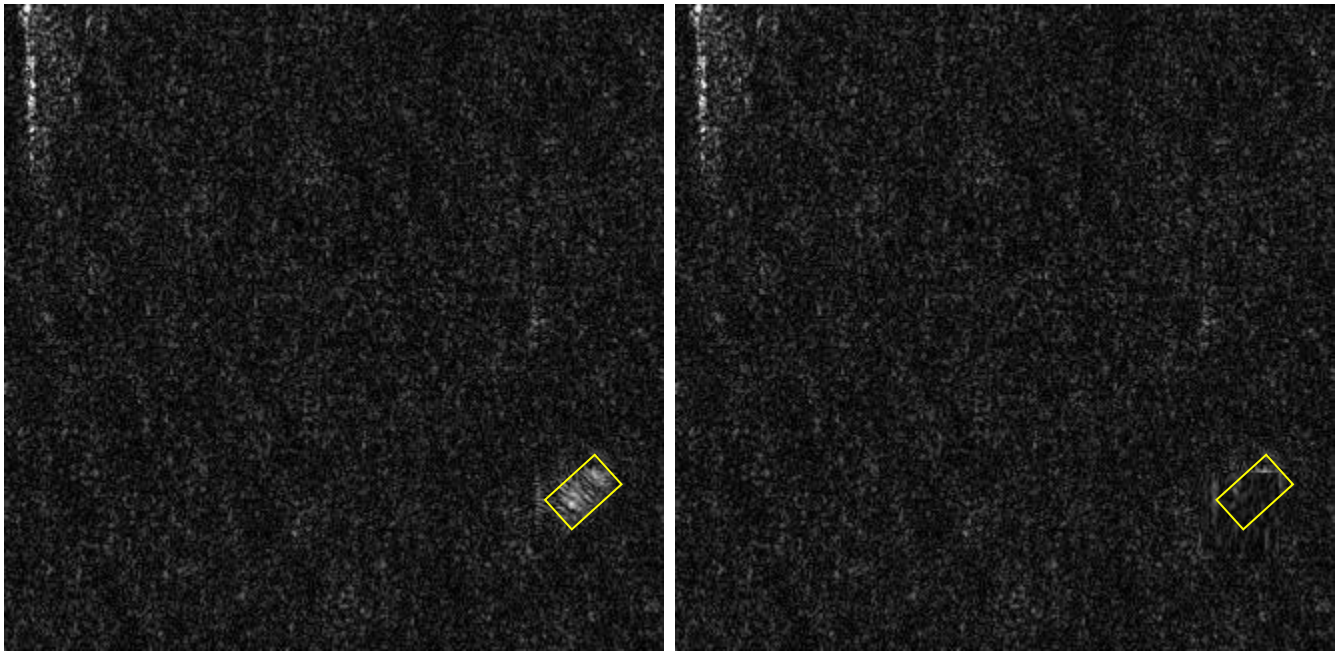

(a) (b)

Fig. 7: Full-resolution particular of the TerraSAR-X image relevant to the ghost marked in red in Fig. 6: original (a) and filtered (b) image.

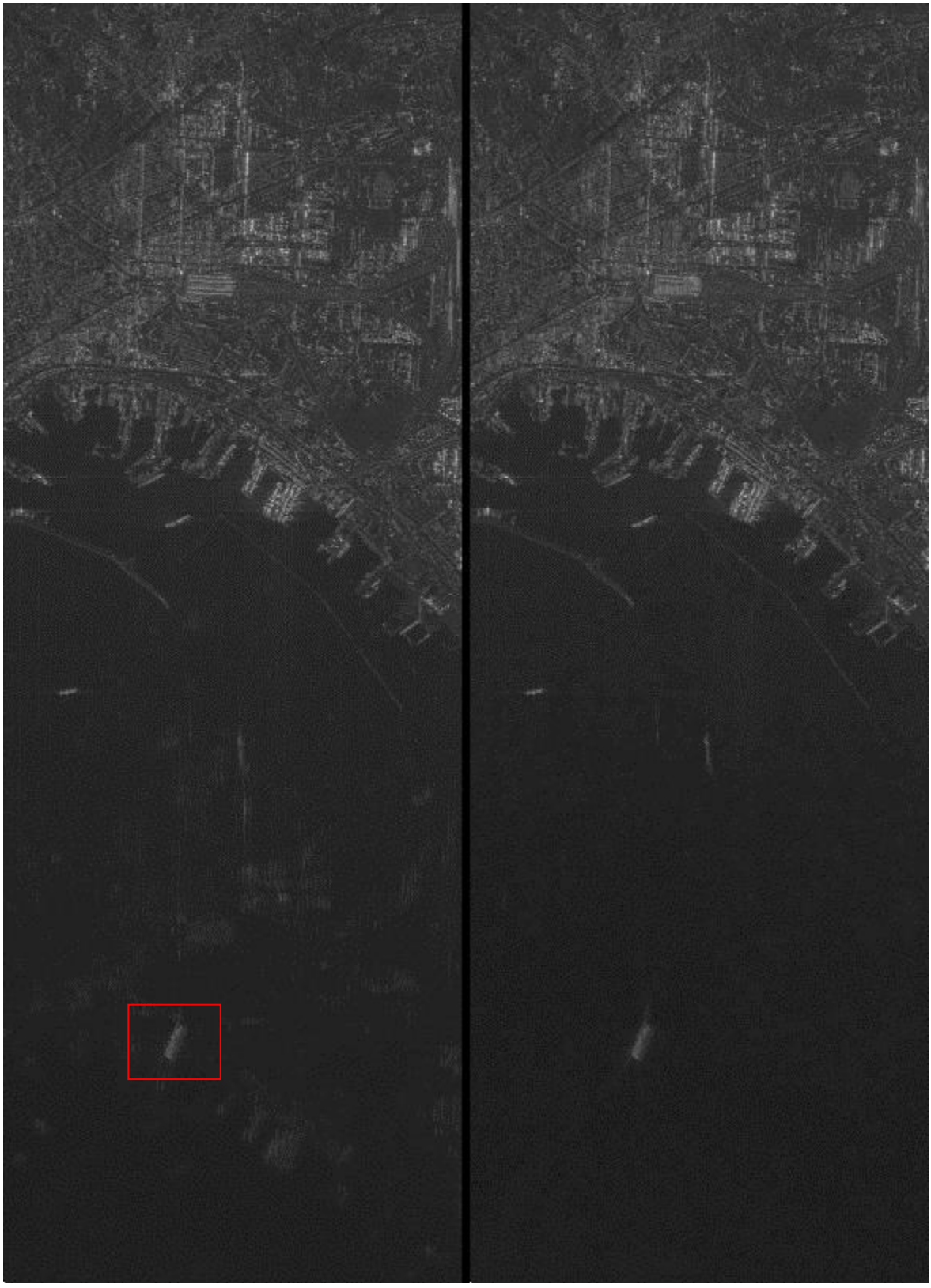

(a) (b)

Fig. 8: Original Cosmo/SkyMed image of the gulf of Naples (a) and its filtered version (b) (a spatial multilook of 6x6 pixels is applied). Ambiguities due to buildings and man-made areas are visible all over the sea surface in (a), while they are strongly attenuated in (b).

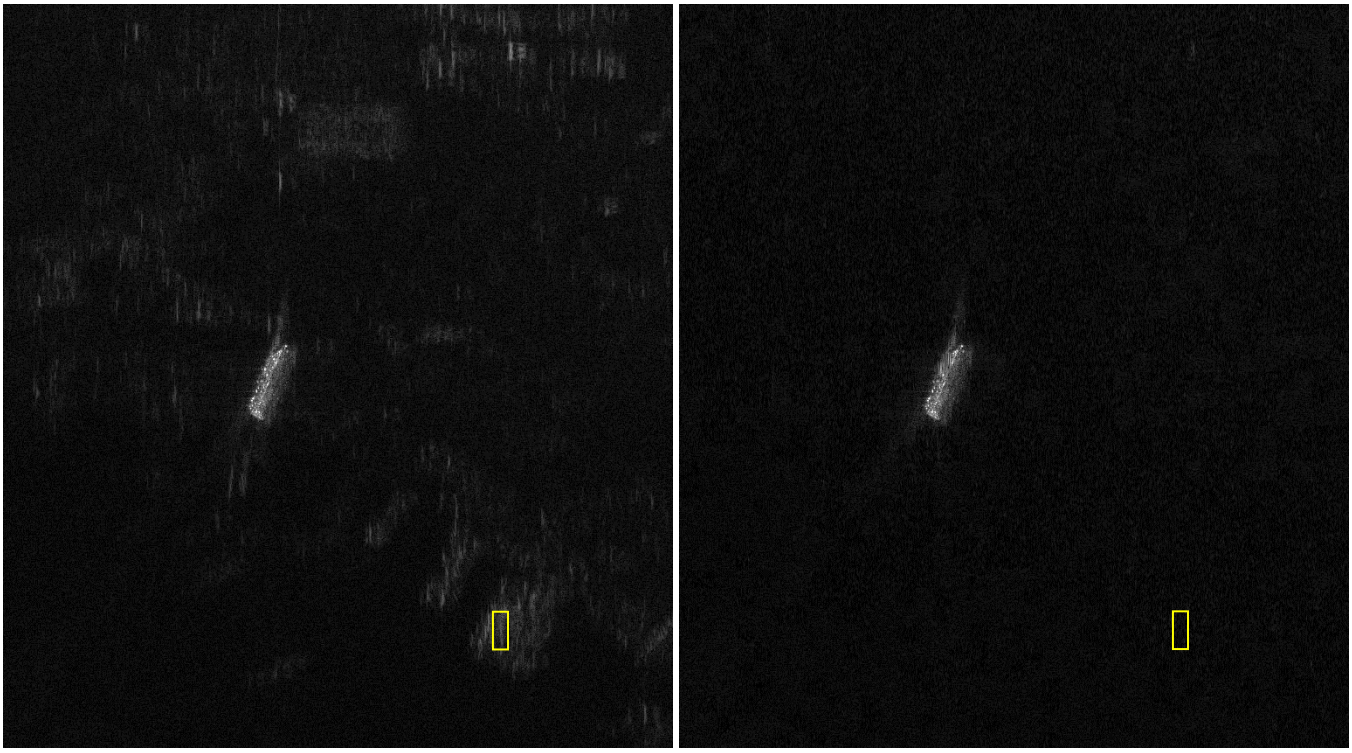

(a) (b)

Fig. 9: Full-resolution particular of the Cosmo/SkyMed image in Fig. 8: original (a) and filtered (b) image.

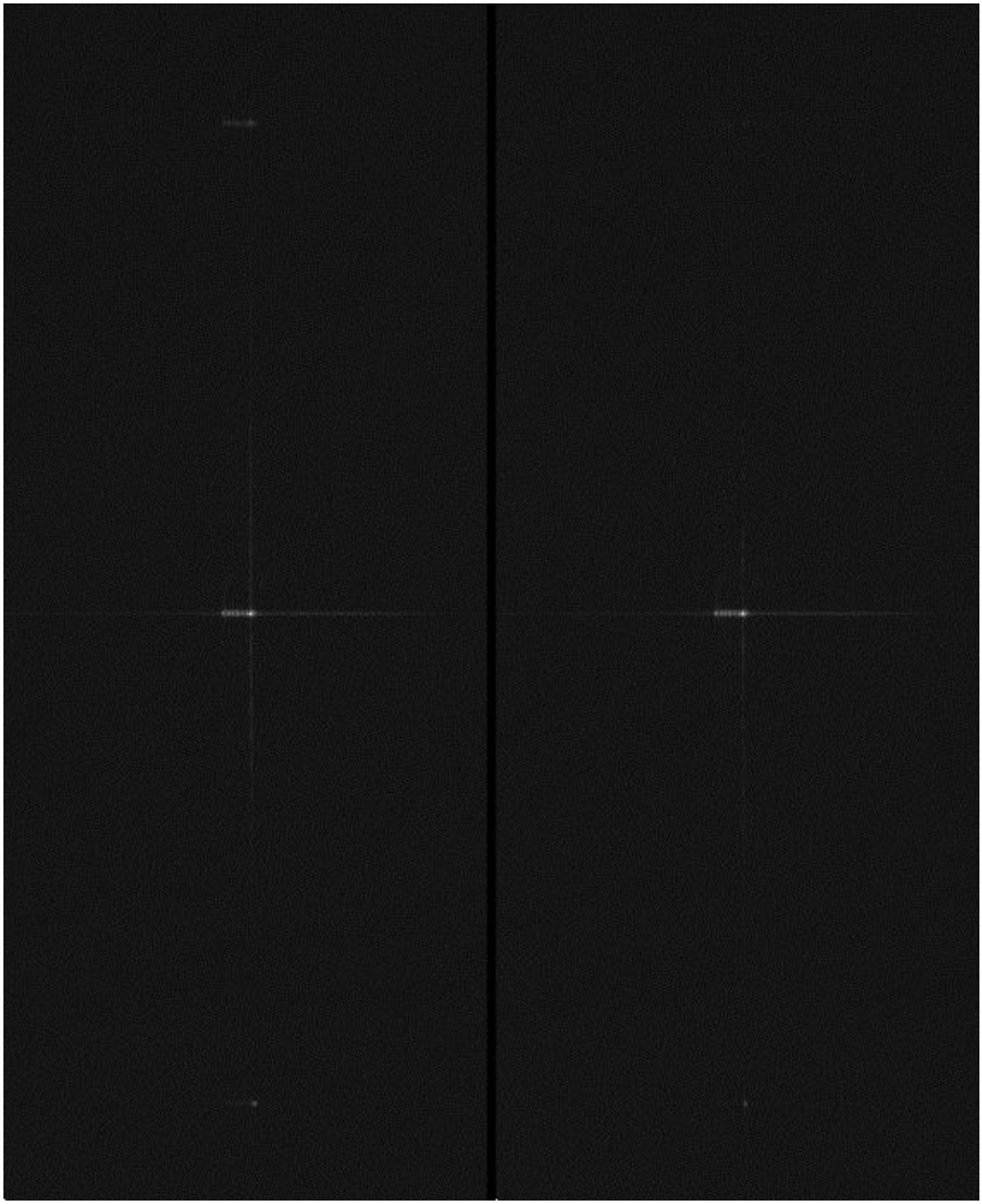

(a) (b)

Fig. 10: Original Cosmo/SkyMed image acquired close to the coast of Malta (a) and its filtered version (b) (a spatial multilook of 8x8 pixels is applied). The ambiguities due to both sidelobes are visible in (a) on each side of the unambiguous ship located in the center of the scene; both ghosts are strongly attenuated in (b), although they are still visible.

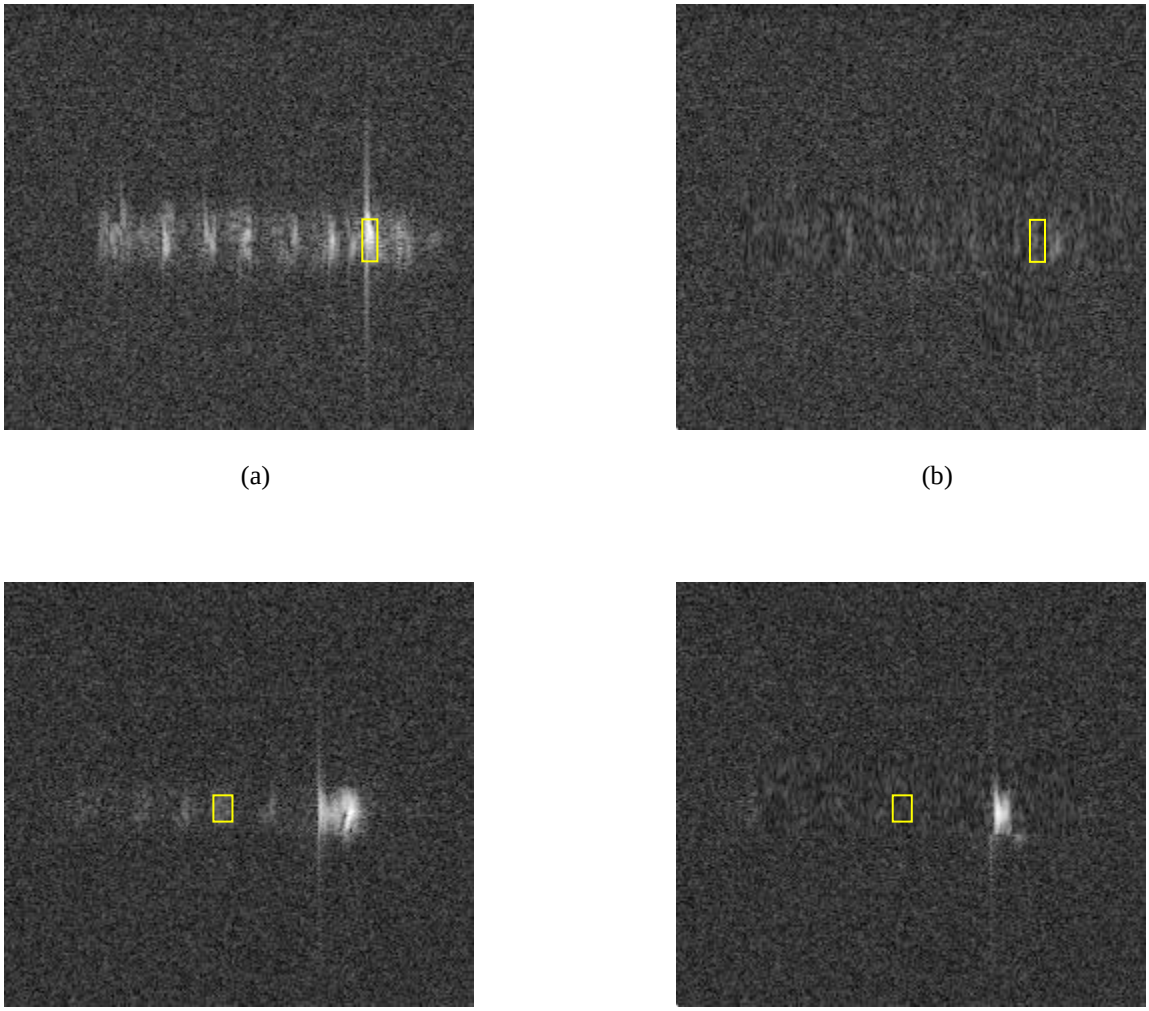

(a) (b)

(c) (d)

Fig. 11: Full-resolution particular of the Cosmo/SkyMed image in Fig. 10: top ghost original (a) and filtered (b) image; bottom ghost original (c) and filtered (d) image.

TABLE II
PERFORMANCE EVALUATION INDEX: GHOST-TO-BACKGROUND RATIO

	Original	Filtered	Ghost attenuation
TerraSAR Algeria	10.7 dB	3.8 dB	−6.9 dB
TerraSAR Naples	8.0 dB	2.2 dB	−5.8 dB
Cosmo Naples	15.5 dB	0.1 dB	−15.4 dB
Cosmo Malta (top)	24.8 dB	2.9 dB	−21.9 dB
Cosmo Malta (bottom)	9.8 dB	1.0 dB	−8.8 dB

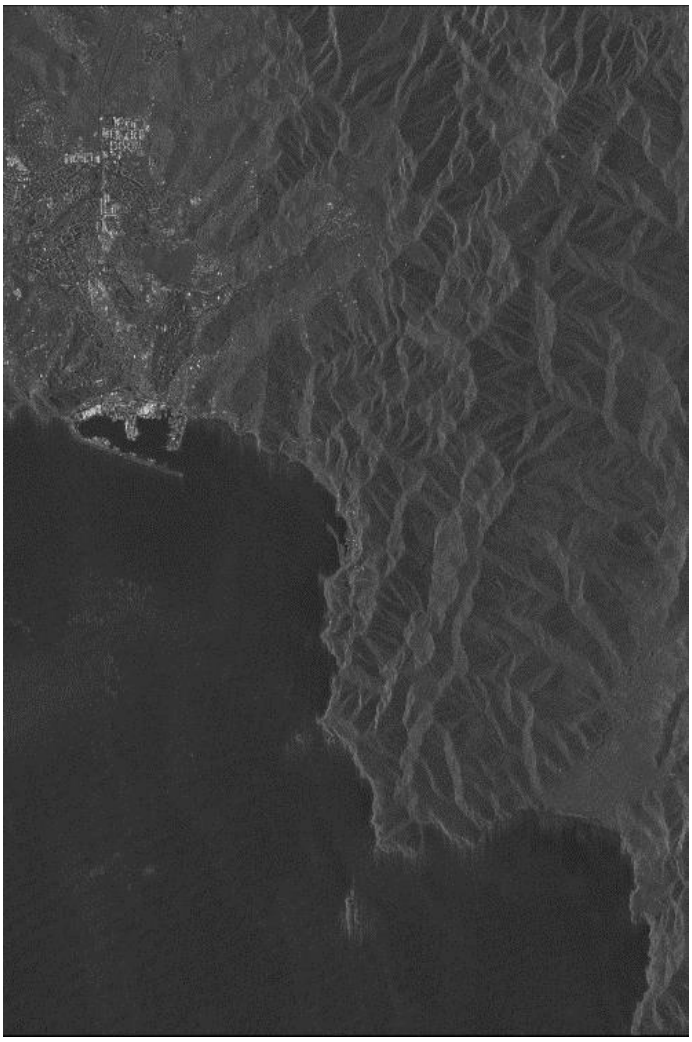

Fig. 12: TerraSAR-X image of the coast of Algeria filtered with the filter TF in (18) (a spatial multilook of 8x8 pixels is applied). The original image is the one reported in Fig. 4 (a). It can be noted that no ambiguity reduction is obtained in this case.

(a)

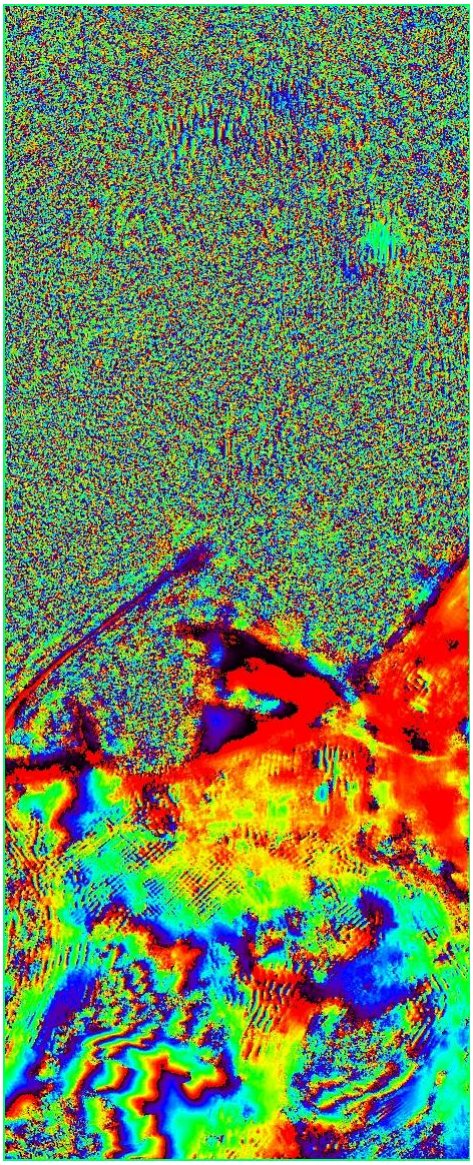

(b)

(c)

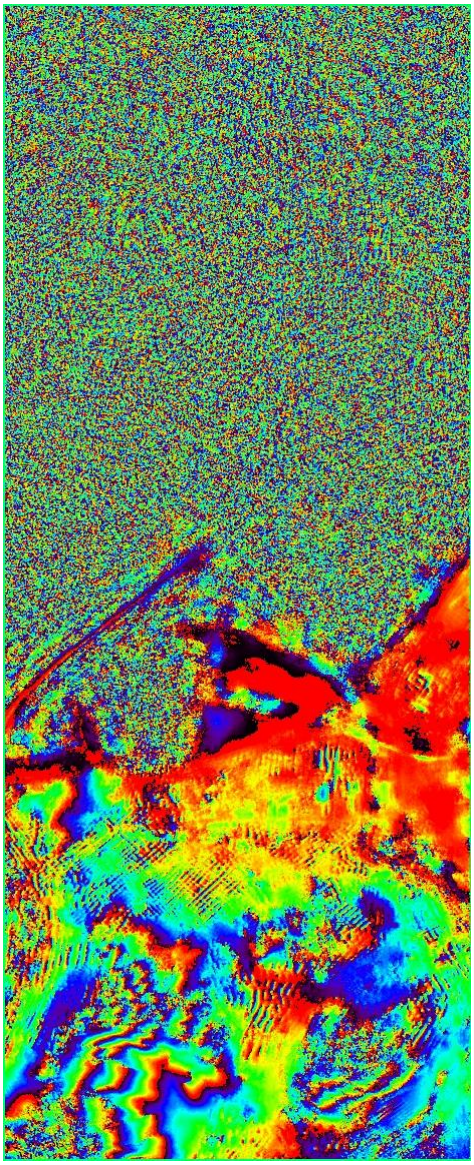

(d)

Fig. 13: TerraSAR-X image pair of Crotone: amplitude of original master image (a), interferogram obtained from the original image pair (b), amplitude of the filtered master image (c), and interferogram obtained from the filtered image pair (d). A spatial multilook of 4x4 pixels is applied.